Controlling the number of layers of Mo-grown CVD graphene through the catalyst thickness

Sacco, Leandro Nicolas; Dobrowolski, Artur; Boshuizen, Bart; Jagiełło, Jakub; Pyrzanowska, Beata; Łaszcz, Adam; Ciuk, Tymoteusz; Vollebregt, Sten

DOI
10.1016/j.diamond.2025.112195

Publication date
2025

Document Version
Final published version

Published in
Diamond and Related Materials

Diamond & Related Materials 154 (2025) 112195

Contents lists available at ScienceDirect

Diamond & Related Materials

journal homepage: www.elsevier.com/locate/diamond

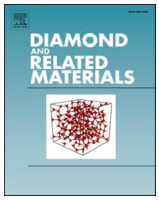

Controlling the number of layers of Mo-grown CVD graphene through the catalyst thickness

Leandro Nicolas Sacco [a,*], Artur Dobrowolski [c], Bart Boshuizen [b], Jakub Jagiełło [c], Beata Pyrzanowska [c], Adam Łaszcz [c], Tymoteusz Ciuk [c], Sten Vollebregt [a]

[a] Department of Microelectronics, Faculty of Electrical Engineering, Mathematics and Computer Science, Delft University of Technology, 2628 CD Delft, the Netherlands
[b] Department of Chemical Engineering, Faculty of Applied Sciences, Delft University of Technology, Van der Maasweg 9, 2629 HZ Delft, the Netherlands
[c] Łukasiewicz Research Network - Institute of Microelectronics and Photonics, Al. Lotników 32/46, 02-668 Warsaw, Poland

A B S T R A C T

Depending on the applications based on graphene, single-layer or few-layer graphene would be more beneficial. Ideally, graphene could be nucleated directly with the required thickness. However, some aspects related to graphene thickness and uniformity control still need to be solved. This work aims to better understand graphene formation using Mo thin films as a catalyst. The grown graphene films were characterized using SEM, TEM, XPS, AFM, standard Raman spectroscopy and 3D Raman surface imaging. A correlation between the catalyst thickness and the number of layers is established. All the characterization techniques show that the number of graphene layers inversely scales with the Mo catalyst thickness used for the graphene synthesis. Then, by simply adjusting the catalyst thickness, the number of graphene layers can be engineered from few-layer graphene (FLG) up to multi-layer graphene (MLG). A pinhole distribution of 1 % was detected on the films synthesized on 50 nm and 100 nm Mo thicknesses after the catalyst was etched. On the synthesized FLG (500 nm Mo), no holes were observed on the surface film after the etching process and even after a transfer onto another substrate. These results can enable the formation of FLG with a controlled thickness and good uniformity.

1. Introduction

Chemical vapour deposition (CVD) on metal catalysts is regarded as the most suitable approach to developing high-quality graphene-based industrial applications due to its scalability and good control over the number of layers and structural quality [1]. To fully exploit the astonishing theoretical properties of graphene, the metal catalyst needs to be removed after synthesis. Different wet/dry approaches have been developed to transfer the graphene onto arbitrary substrates [2]. Many efforts were devoted to precisely controlling the reproducibility and cleanness of the transfer [3]. However, the transfer processes are still challenging because they can induce wrinkles, cracks, or material contamination. The scalability is still a major drawback, especially for suspended graphene films. Alternatively, graphene transfer-free methods were developed that can be divided into different groups: catalyst-free graphene growth [4], metal-free [5], and sacrificial metal-assisted growth via CVD [6], which can be also called the transfer-free method [7].

Many factors given by the metal catalysts and substrate characteristics can influence the graphene crystal lattice formation. In particular, for the metal-catalyst-based CVD approaches, the carbon solubility on the metal, metal thickness [8], the surface roughness [9], the topological defects of the catalyst, like the grain boundaries [10], and kink sites [11] are critical to graphene formation. Various metals have been employed to catalyze graphene growth [12]. Copper (Cu) is the most common metal for single-layer graphene synthesis because a surface self-limiting [13] growth takes place due to the low solubility of Carbon (7.4 ppm at 1020 °C) [14]. However, for synthesis on a wafer scale, some drawbacks to its implementation arise due to the relatively low melting point of Cu [15], and the large mismatch between thermal-expansion coefficients of graphene, Cu and Si [16]. Nickel (Ni) is widely used as a catalyst for the synthesis of few-layer graphene up to multilayer graphene. The high carbon solubility on Ni (2584 ppm at 1000 °C [17]) leads to a graphene formation given by a sequence of saturation and segregation/precipitation processes [18]. The main disadvantage of graphene grown on Ni is the large graphene layer variations at the microscale, which relates to the large solid solubility of the metal [19].

Molybdenum (Mo) is a suitable metal catalyst for graphene synthesis. The advantage of Mo is its high melting point (2623 °C), a closer thermal expansion coefficient to that of Si and graphene compared with Ni and Cu [20], and a carbon solubility in Mo of 700 ppm at 1500 °C [14] which can allow the synthesis of single-layer up to MLG [21].

* Corresponding author.
E-mail address: l.n.sacco@tudelft.nl (L.N. Sacco).

https://doi.org/10.1016/j.diamond.2025.112195
Received 13 November 2024; Received in revised form 8 March 2025; Accepted 10 March 2025
Available online 14 March 2025

Therefore, the use of Mo catalyst needs to be further investigated as an alternative catalyst that can be considered up to some extent as compatible with the mature complementary metal oxide semiconductor (CMOS) technologies [22]. Under this context, various devices were developed using Mo as a catalyst for MLG synthesis [23–25] using a transfer-free approach [26].

However, there are still many issues to address regarding the uniformity of graphene film on the microscale synthesized using Mo. On one hand, from a synthesis perspective, Zou et al. [27] proposed that transitional metals such as Mo, during the CVD process, can form carbides like Mo_2C that serve as a catalyst for the graphene formation, furthermore, the carbide layer can hinder the segregation/precipitation effect during cooling stages that can lead to the non-uniform synthesis of graphene layers within the sample [28]. On the other hand, recently, Kizir et al. [29] shows that Mo thin films sputtered on a substrate required pinholes that act as catalytic sites for the MLG synthesis, compromising the synthesized MLG structure.

In the present work, a systematic study was performed analysing the structure of graphene films synthesized by the CVD process using as a catalyst Mo thin film with different thicknesses on SiO_2/Si substrates, where Mo was subsequently etched using hydrogen peroxide. The graphene structure was accessed in terms of the number of layers and pinhole density by diverse characterization techniques like scanning electron microscopy (SEM), atomic force microscopy (AFM), transmission electron microscopes (TEM), Raman spectroscopy, optical microscopy and X-ray Photoelectron Spectroscopy (XPS). The adopted metal catalyst variation reveals that the number of graphene layers can be varied from a single or bi-layer film (using a 500 nm Mo thick catalyst) up to >25 graphene layers (using a 50 nm Mo thick catalyst). Furthermore, holes observed after transfer are affected by the thickness and appear absent when 500 nm Mo is used as the catalyst. Overall, the present work aims to investigate the influence of Mo thin films on synthesized materials and give a route towards the fabrication of graphene films with tuneable structural properties adopting a transfer-free approach or transferring the graphene onto a target substrate.

2. Results

The main goal of this study is to analyse the influence of the catalyst thickness on the graphene films grown by CVD on Mo, in terms of the number of graphene layers and the density of structural defects present in the film surface. Furthermore, the impact of the transfer-free approach and the graphene transfer onto a target substrate on the structural defects is estimated. Different structural characterization techniques were then performed, such as Raman spectroscopy, XPS, TEM, SEM, and AFM.

2.1. Number of graphene layers depending on the Mo catalyst thickness

Fig. 1 shows the Raman spectra from graphene films transferred onto a target SiO_2/Si substrate. From the Raman spectra, the most prominent peaks of the graphene can be identified; the so-called “G band” can be found approximately at 1580 cm-1 wavenumber; it is mainly activated due to an electron-phonon coupling interaction. The “D-band” refers to the defects induced by the graphene layer, typically found at 1350 cm^{-1}. The “2D-band” results from two-phonon processes and can be found at approximately 2700 cm^{-1}. The 2D Raman peak is associated with graphite-like materials. The intensity ratio of the G and 2D bands (I_{2D}/I_G) is often used to discriminate between single-layer graphene, FLG or a graphitic structure. However, for FLG with more than five layers, the Raman spectrum is barely discernible from that of nano-graphite/graphite [30,31]. Then, for graphene stacking containing >5 layers, another approach is required to precisely determine the number of layers [32]. The intensity ratio of the D and G bands (I_D/I_G) quantifies the amounts of defects on the synthesized graphitic structures.

For the three used Mo catalyst thicknesses, the I_{2D}/I_G and FWHM(2D)

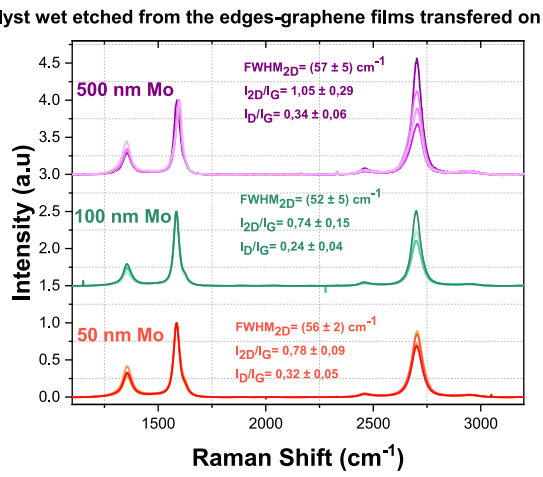

Fig. 1. Raman spectra were measured on transferred graphene films on SiO_2/Si substrates. The MLG films were grown using Mo catalyst with different thicknesses (50 nm, 100 nm, and 500 nm). The Raman measurements were performed at 5 different positions in each sample.

average values are indicated in Fig. 1, showing that the synthesized material results in turbostratic films [33]. The extracted FWHM, can be used also as standard way for determining the number of layers [34]. For instance, in the case of turbostratic graphitic structures 2D band of turbostratic graphitic structures can be decomposed with a Lorenztian single peak indicating a weak interaction coupling between the graphene adjacent layers [41] but with almost double FWHDM compared with that one of the SGL (typically of 25 cm^{-1}). Herein, extracted FWHM is around 50–62 cm^{-1} [35], characteristic of the turbostratic structure [35]. In contrast, for graphite, the D band is not Raman active but becomes sensitive for multi-layers with significant defects [36]. The I_D/I_G values for the three catalyst thicknesses statistically overlap around 0.24–0.34, reflecting that the amount of defects is equivalent, and the three graphene films have relatively good quality for Mo-grown graphene, which typically have I_D/I_G ratios of 0.2–0.3 [19].

AFM was used to determine the graphene sheets thicknesses. The height between the transferred graphene sheets and the targeted substrate was measured. The number of the graphene layers was estimated based on a literature value and TEM estimation of graphene layers distance [37]. Fig. S1 summarized the procedure to calculate thickness of the transferred graphene using AFM. The inspected areas were close to graphene films edges. Then, five height profiles were measured in each graphene film. Table 1, summarizes the graphene thicknesses and number of layers depending on the catalyst thickness, extracted from AFM measurements. These results give a trend on the number of layers but offset error in the measurement can arise due to tip-surface interactions, image feedback settings and/or surface chemistry as was previously reported by Shearer et al. [37]. Therefore, other techniques need to be also considered to get a more accurate indication of the graphene thickness.

Due to the difficulty of determining the number of graphene layers by conventional microscopy measurements [38], a 3D Raman surface imaging model was used to determine the number of graphene layers [39,40] and generate a three-dimensional image, assuming a constant

Table 1
Graphene films thickness and number of graphene layers extracted from AFM measurements.

Mo catalysts thickness for graphene growth [nm]	Graphene film thickness [nm]	Number of graphene layers
50	7.9 ± 2.1	22 ± 6
100	7.1 ± 1	20 ± 3
500	2.4 ± 0.4	6.6 ± 1

literature interlayer distance in MLG [41,42]. It relies on the principle of a reduced Raman signal of the substrate underneath the graphene when passing through the material. The thicknesses of the graphene films were calculated afterward.

Fig. 2 summarizes the results obtained by implementing the shadow method analysis [40] to determine the number of graphene layers of each film grown using different catalyst thicknesses. The optical images of the transferred graphene films using 50 nm and 100 nm of Mo catalyst, Fig. 2.a-b have a similar contrast and some brighter areas in the submicrometre scale. The optical contrast of the graphene film grown using a 500 nm thick catalyst, and subsequently transferred on a SiO_2/Si substrate as shown in Fig. 2.c, is quite different comparing with the graphene films grown using thinner Mo catalysts. In this case, the graphene film seems more uniform (similar optical contrast) with some darker areas indicating some protuberances in the micrometre scale. As the Mo catalyst thickness increases to synthesize the graphitic structures, the density of scattered circular protuberance decreases, causing the darkening of the image and the surface to become more homogeneous and flatter.

For a more detailed analysis, two points (P1 and P2 from Fig. 2.a-f) were selected from each map. The first point (P1) indicates the typical area of the sample (areas of flattening), the second point (P2) indicates depressions in the surface. Representative points selected in this way allow meaningful comparison of individual measurements. For each sample, the selected P1 points coincide with the mean values from the histograms shown in Fig. 2.g-i. For MLG grown on 50 nm and 100 nm thick Mo catalyst, the depressions have up to 9 layers less than the characteristic areas. In a sample grown using 500 nm of metal catalyst, even a single layer may be present in the depression. As can be seen in the three-dimensional visualizations (Fig. 2.g-i), a kind of lumps are spread over the surface of each sample. Although the lumps affect the shading of the image, they cannot be unambiguously associated with graphene layers, as they have not been shown to affect the nature of the graphene spectrum, as shown by supportive Raman analysis (Fig. 3.a-b). The exception is the sample grown on 500 nm of Mo catalyst, where a single lump (marked by blue arrow in Fig. 2.f) does indeed affect the shape and position of the modes, which may indicate that it represents an additional graphene layer(s) (Fig. 3.c).

The Raman spectra of the individual samples do not differ in any particular way. A more in-depth statistical analysis also shows that the positions, shapes, and ratios of the Raman mode intensities are similar in the typical area (P1 point) for each sample, as indicated in Fig. S2 and Table S1.

The 3D Raman analysis showed a significant reduction in the number of layers with increasing Mo catalyst thickness. For seed catalyst thicknesses of 50 nm and 100 nm, the distribution of values can be

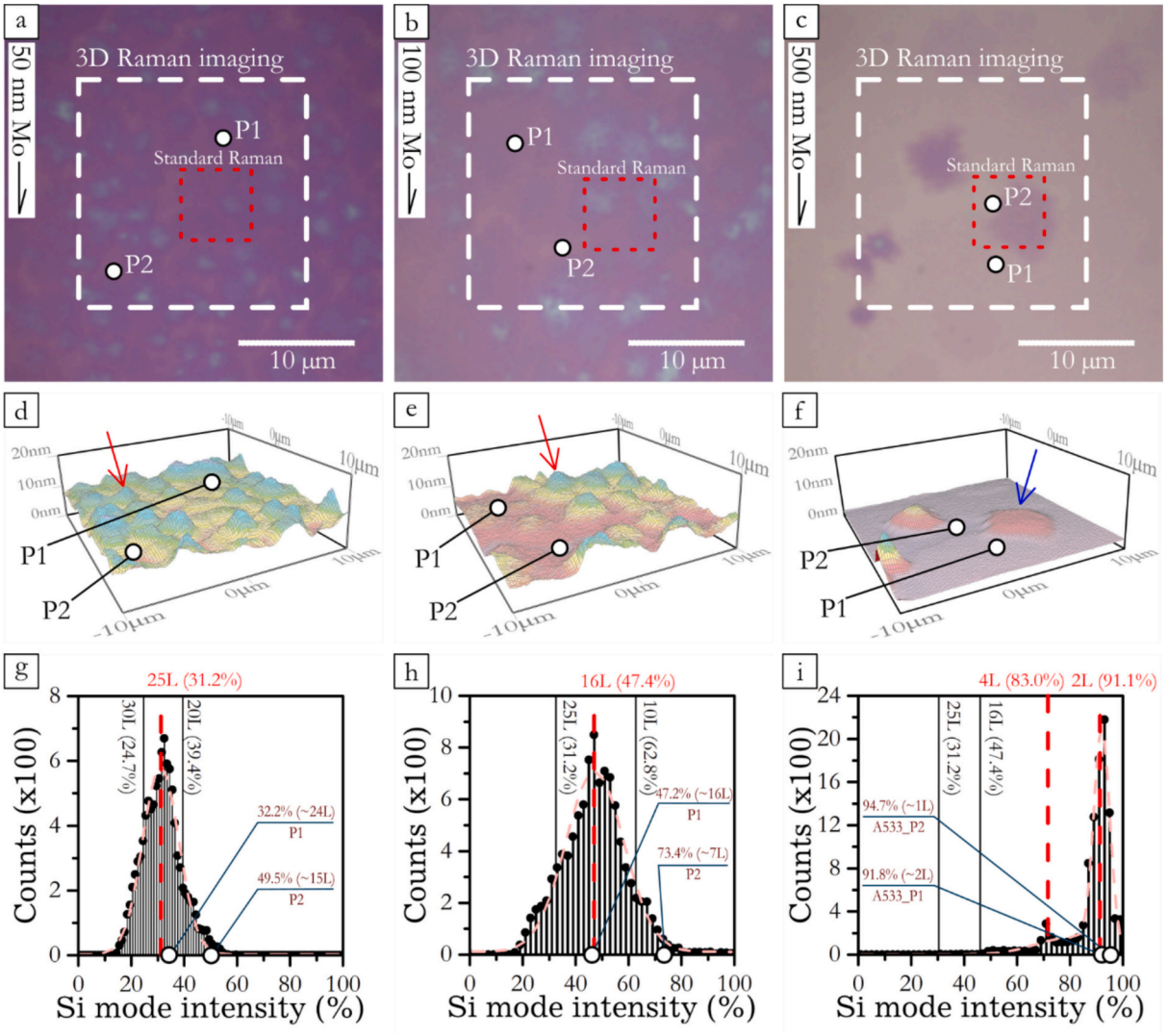

Fig. 2. a-c Optical view of the sample with 3D Raman surface imaging areas (white frame), and supportive Raman spectroscopy (red frame). d-f Effects of high-resolution imaging of Surface topography. g-i results of 3D Raman analysis.

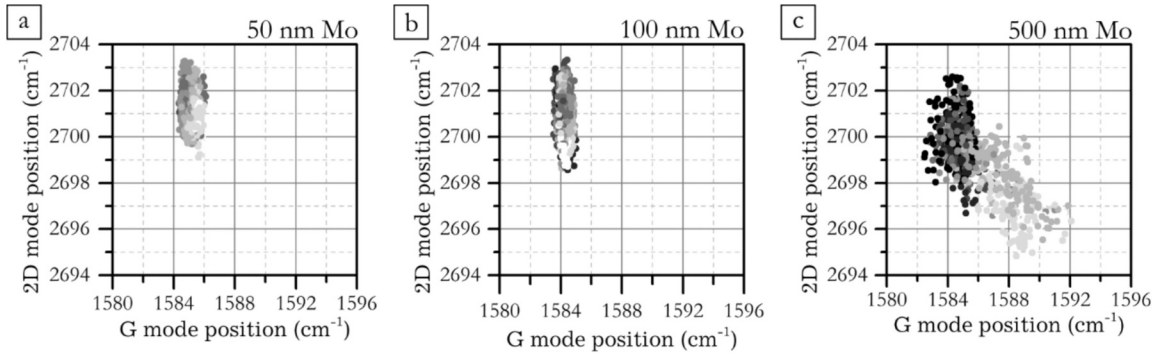

Fig. 3. G and 2D modes position correlation plots for graphene film grown on different Mo catalyst thicknesses: a. 50 nm, b. 50 nm, and c. 500 nm. The grayscale convention represents a situation where a darker shade corresponds to more layers and a lighter shade to fewer layers. The grayscale range is adjusted for each point according to the range of values on the histograms in Fig. 2.g-i. This means that the range of grayscale spread is individual for each case and differs from others.

approximately described by a single bell curve with an expected value of 25 and 16 layers, respectively, as extracted from Fig. 2.g-h, confirming the MLG structure. For the sample grown on 500 nm Mo catalyst, from Fig. 2.i, in the study area, two peaks corresponding to 2 and 4 layers were observed in the distribution, indicating a FLG structure.

Fig. 3 summarizes the G and 2D modes position plots. The correlation plots of graphene sheets grown on 50 nm and 100 nm Mo catalysts (Fig. 3a-b, respectively) in both cases reveal that groups are formed around the G mode position of 1584 cm^{-1} and 2D mode position of 2701 cm^{-1}. Then, the occurrence of lumps marked by the red arrow in Fig. 2.d-e does not appear to affect the shape and properties of the spectrum, probably due to the turbostratic nature of the grown graphene. On the other hand, the graphene sheets grown on a 500 nm thick Mo catalyst present a correlation plot shown in Fig. 3.c with a scattered cloud, separated on a gray scale-mode shift that can be related to the number of FLG. The simplified concept for gray scale markers points in Fig. 3.a-c is that the darker the shade, the more layers and the lighter the shade, the fewer layers. In this case, the presence of the lump marked by the blue arrow in Fig. 2.f causes changes in the positions of the G and 2D modes, and it can be argued that this represents additional graphene layers (the darkest points in Fig. 3.c). On the other hand, for the P2 point in Fig. 2.c and .f, that is, the area of depression, there is an apparent separation of points from the primary cloud, clearly correlated with fewer layers (brighter signal of the underlying modes). It is important to highlight that in both Raman systems, the results extracted from the spectrum are equivalent.

TEM analysis can be considered as a direct measurement to quantify the number of graphene layers. FIB has been used in preparing TEM specimens for cross-sectional type inspection of the graphene sheets. However, TEM observations involved a lamella fabrication that can be time-consuming for their preparation, and the measurements are more localized in space.

The thickness measurements were taken at different locations of the lamellas. Fig. S3 shows the HR-TEM micrograph of the FLG synthesized with the thickest Mo catalyst; the measured interlayer distance is 0.36 nm and is equal for all the analyzed samples, as expected in turbostratic graphene. This is also in agreement with the extracted FWHM. Fig. 4 the detailed view of the graphene films synthesized with different Mo catalyst thicknesses. These observations allow us to determine the film thickness and the number of layers. The number of layers varies significantly within the sample synthesized with 50 nm of Mo catalyst. Then, the number of layers varies between 15 and 18 layers, and 5 and 6 for the graphene films synthesized using 100 nm and 500 nm of Mo catalyst, respectively.

Then, TEM observation is an evident comparative technique to assess the validity of a relatively simple and non-invasive method like AFM measurements and the 3D Raman surface imaging model for estimation of the thickness of graphene layers. Fig. 5 shows the number of graphene layers extracted with different approaches depending on the Mo catalyst thickness used to grow the graphene films. The variations are not attributed to measurement technique but a material property. This multi-characterization approach also aims to give a notion of the measurement complexity of each technique and the degree of accuracy that can be obtained. The measurements were not performed at the same locations for the three techniques. In that case, a more direct comparison could be realized. However, the accumulated results reveal that the three techniques follow the same trend on the dependency of the number of graphene layers and the catalyst thickness. Collectively, this

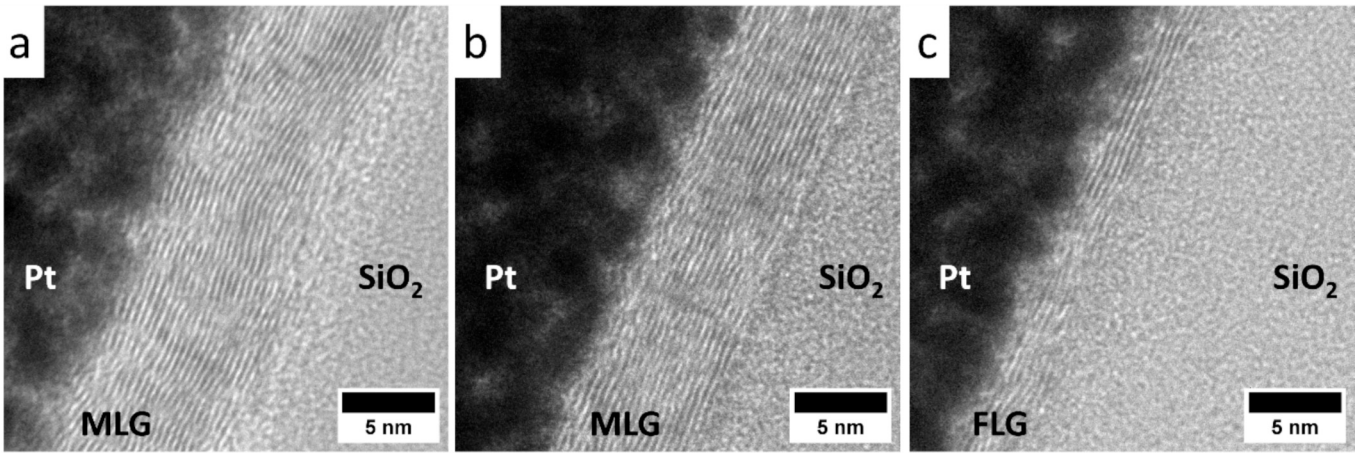

Fig. 4. HR-TEM images of the graphene films synthesized using different Mo catalyst thicknesses: a. 50 nm, b. 100 nm and c. 500 nm.

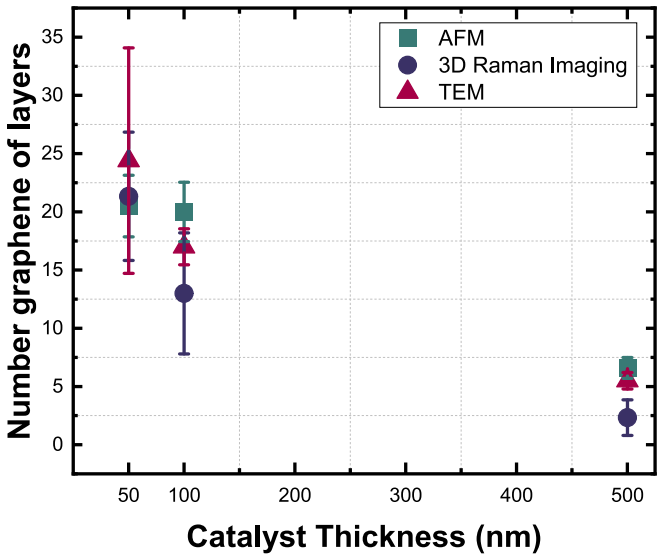

Fig. 5. The number of graphene layers as a function of the Mo catalyst thickness extracted from different characterization techniques like AFM, 3D Raman Imaging, and TEM.

analysis provides valuable information to better understand graphene formation and the influence of catalyst thickness on the CVD process.

2.2. *Graphene morphology characterization on the catalyst after the transfer-free process and after transferring*

Fig. 6 shows the Raman spectrum performed on graphene films still with the metal catalyst underneath growing on 50 nm, 100 nm and 500 nm catalyst thicknesses. The I_D/I_G intensity mean values overlap for the three catalyst thicknesses in the range of 0.23–0.26, reflecting a relatively good graphene quality for Mo-grown graphene [43]. The collected noisy signal on the sample with 500 nm Mo thickness can be attributed to a wider dispersion of the reflected laser beam on the thick catalyst and the thinner graphene film (the number of the layers does not seem to be the cause since the Raman spectrum in Fig. 1 does not have such

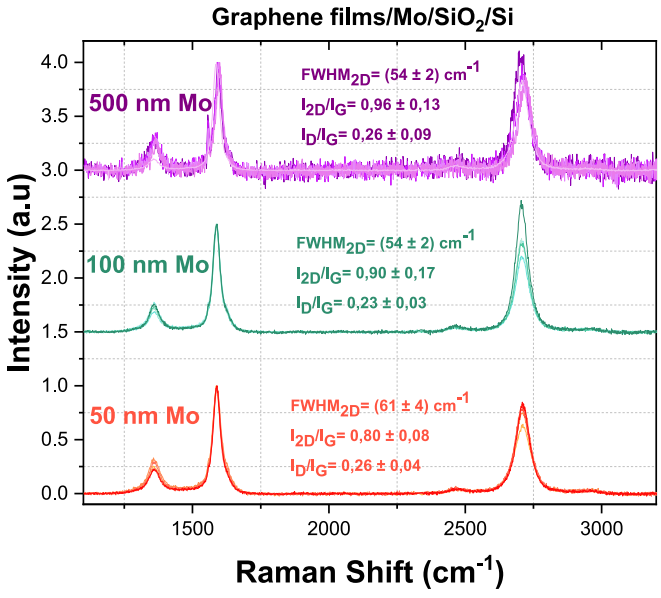

Fig. 6. Raman spectra were measured on synthesized graphene films using Mo catalysts with different thicknesses (50 nm, 100 nm, and 500 nm). The Raman measurements were performed at 5 different positions in each sample.

characteristics and the same number of graphene layers are expected after the transfer process). The noisy signal leads to a higher error value for the calculation of the bands' intensity ratios for this sample.

Fig. 7 shows the top-view SEM of the graphene films' growth with the catalyst underneath. In the three samples, the SEM images show a facetted structure of the graphene layers that may follow the Mo_2C surface. The grains' domains are on the 10–100 s nanometer scale. No holes were detected in the three inspected samples, revealing that under the presented catalyst deposition and synthesis conditions, the presence of holes is not necessary to promote the MLG synthesis, in contrast with the results reported by Kisir et al. [29].

From the AFM images shown in Fig. 8, the R_a value was extracted. For the three catalyst thicknesses, the R_a values are in the range of 4.5–6.0 nm. Despite the grain structure of the graphene films induced by the catalyst reorganization during the CVD process, no pinholes were detected with both inspection techniques. This result indicates that the grain boundaries probably work as nucleation sites for carbon diffusion into the catalyst [44].

The Mo catalyst underneath the graphene films was etched using a wet approach. In the first attempt, the metal catalyst was dissolved, and the synthesized graphene landed on the native substrate. The idea is to monitor the structural properties of the graphene at every step of the final transfer process and compare it with the transfer-free approach. The Raman spectrum of the graphene films and the surface micrograph obtained by SEM and AFM are shown in the supporting information (see Figs. S4, S5 and S6, respectively). In terms of D/G intensity ratios, no significant differences are observed in the graphene films before and after the etching steps.

The FLG grown using a 500 nm Mo catalyst, shows a less intense band around 1145 cm^{-1}. However, this band relates to the presence of oxidised Mo catalyst, as shown in Fig. S4.b. In this case, the Raman analysis was performed on the FLG grown on 500 nm of Mo catalyst in the range of 100–1100 cm^{-1}, where the Raman spectrum shows the characteristic peaks of MoO_3 in stretching and deformation modes in the range from 100 to 1000 cm^{-1}, as it has been previously reported [45–47]. This is a clear indication that for this catalyst thickness, the etching process was not fully effective in dissolving the catalyst underneath the graphene layer(s).

From Fig. S5, interestingly, it is clear that the 50 nm and 100 nm catalyst etching process led to the formation of some holes in the MLG structure (Fig. S5.a-b) and non-catalyst residues are observable. In contrast, the etching process on the 500 nm catalyst induces many cracks, as observed in Fig. S5.c Remarkably, this kind of structure was only detected during the graphene release phase because no cracks of the same length were observed after the transfer process (Fig. 8.c and Fig. S8). Nevertheless, no evidence of holes is found in the graphene layers lying on the partially dissolved catalyst. The presence of catalyst residues after the etching step was confirmed for all the thicknesses by XPS data analysis, as shown in Fig. S7 and Table S2, which summarizes the atomic concentration of the elements C, O, Si and Mo. Particularly, the graphene grew on a 500 nm thick catalyst and still has approximately 5 % Mo compounds after the etching step.

Herein, it is important to point out that the transferring process prevents the formation of large cracks. Herein, we hypothesized that the DW addition slows down the catalyst etching and releases the graphene sheets. On the contrary, if the transfer is not promoted, the etching still occurs and affects the graphene sheet structure. The timing of this procedure might be very important, and of course, it is highly dependent on the catalyst amount that needs to be etched. The etching dynamic is outside of the scope of this work, but it is interesting to pointed out that research can be executed in this direction to get better insights into the catalyst etch and graphene structure.

Fig. S6 shows the AFM scans and the R_a values obtained at three different locations. The AFM scan shown in Fig. S6.c was performed outside regions with cracks. The Ra values for all the analyzed are higher than the obtained values on the graphene films with the catalyst

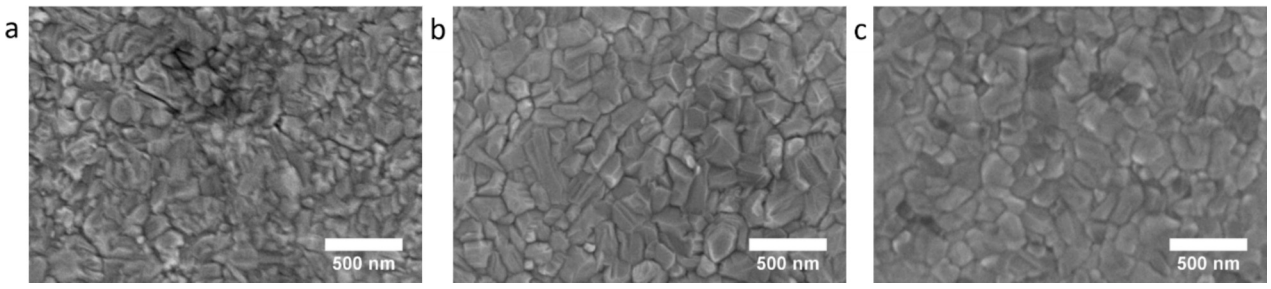

Fig. 7. SEM top view micrographs of graphene films grown via a CVD process using as Mo catalyst with different thicknesses: a. 50 nm, b. 100 nm, and c. 500 nm.

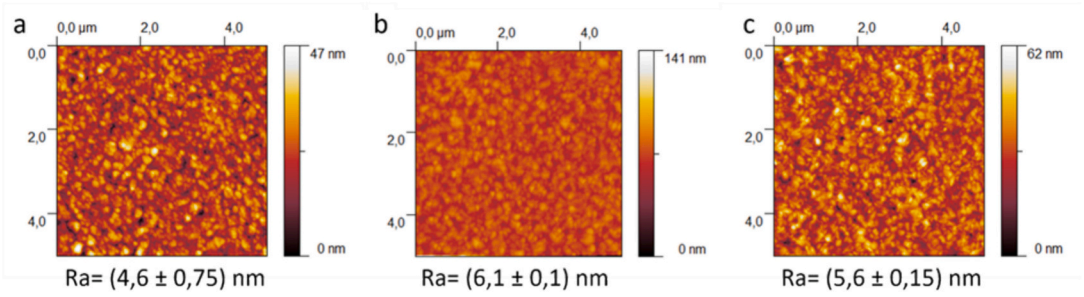

Fig. 8. AFM micrographs of MLG grown via a CVD process using as Mo catalyst with different thicknesses: a. 50 nm, b. 100 nm, and c. 500 nm. The average Ra value obtained from 3 scans performed at different spots is indicated in each sample.

underneath. This can be attributed to the deformations induced during the catalyst wet etching. In summary, under the applied etching conditions, the transfer-free approach induces holes on the MLG films synthesized in thin catalysts (50 and 100 nm thick) and cracks on the FLG synthesized on a 500 nm thick Mo catalyst that was furthermore not fully dissolved. Future studies are required to determine if the catalyst can be fully removed for this thickness.

The graphene films were transferred into a SiO_2/Si after the catalyst was etched. The wet transfer process of graphene onto a target substrate is largely implemented to develop a myriad of applications [2]. The idea is to analyse the influence of the transfer step on the graphene structure. By comparing the Raman spectrum from the transferred graphene films (Fig. 1) and those remaining on the original oxide layer (Fig. S4a), it is possible to infer that the transfer process seems not to induce defects sensitive to the Raman spectroscopy since the D/G intensity ratios are comparable to those calculated when the MLG films were not transferred. Due to the similarity of the bands, it can be concluded that the graphene is not damaged by the etchant. Interestingly, the band detected at the 1150 cm^{-1} wavelength for the 500 nm sample after etching is suppressed after the transferring process. This indicates that Mo oxide residues from the catalyst after the etching process are significantly reduced when the sample is transferred.

XPS depth profiles acquired from the centre of the transferred films were performed, as shown in Fig. 9, to verify the presence of catalyst residues. Fig. 9.a shows the spectrum of the transferred MLG grown on different thicknesses. For the three catalyst thicknesses, the same characteristics peaks are detected, depicting the Si, Mo, C and O peaks [48]. To get more information about the amount of remaining catalyst attached to the graphene films, XPS analysis was acquired during a milling process by Ar ion. Fig. 9.b shows the atomic concentration of the Si, Mo, C and O elements as a function of the etching time. As expected, the C element concentration decreases as the etching process evolves. At the start, the C concentration for the MLG grown on 50 nm and 100 nm is around 91 %. After 120 s of milling, the C atomic concentration is reduced to 50 % and 42 %, respectively. For more details, Table 2 quantifies the spectral components measured by XPS. The FLG grown on 500 nm Mo catalyst has an initial carbon concentration of 57 %, and the C content sharply decreases as the milling process begins. For instance, after 40 s of etching, the remaining C concentration is 8 %, and the Si and O contents present on the substrate are increased much faster than on the graphene grown on thinner catalysts. These results align well with the number of layers as determined in section 3.1.

The catalyst contents are below 1 % in all cases. To monitor the Mo content evolution more clearly during the etching process, Fig. 9.c summarizes the XPS profiles of only the Mo content as the etching process progresses with time. Once again, the MLG films have similar maximum Mo content close to 0.45 %. In the FLG, the Mo content increases after a few seconds of etching the graphene layers, reaching a 1.1 % content; then the Mo content monotonically goes to the minimum detectable value (<0.1 atomic%) as the etching process evolves. In all cases, the XPS profiles indicate that some residues of the sacrificial Mo catalyst layer not only remain after the catalyst etching as was previously reported [49] but also persist after the transfer process. This could indicate that some Mo is embedded into the graphene layer.

Fig. 10 and Fig. 11, respectively, show the SEM and AFM micrographs of the graphene films after the transfer process. In both sets of figures, it is possible to identify that the MLG grown using 50 nm and 100 nm have holes in the surface, which it is not the case for FLG grown using 500 nm of Mo catalyst. This is also confirmed in Fig. S8 where an SEM image is shown in a lower magnification. Here, compared with Fig. S5c, no cracks or failures are detected after transferring the FLG. In Fig. 8.a-b, the holes on the MLG can be identified by the bright edges. The microscope beam locally charges the exposed surface of the dielectric SiO_2 layer on the target substrate. In addition to the holes, many wrinkles can be observed in both samples. In contrast, Fig. 10.c and Fig. S8 do not reveal the presence of charged areas induced by holes in the graphene structure.

The AFM images also confirmed the presence of holes in the MLG synthesized on 50 nm and 100 nm Mo thick catalyst, as shown by the black regions in Fig. 11.a-b. Two profiles were measured in each AFM scan, which also depicted the hole position. In Fig. 11.c, no holes are observable; also, the two representative profiles have height differences only induced by wrinkles in the graphene film surface. In all cases, the Ra significantly decrease compared with the graphene films that remain on the catalyst (Fig. 8) and the graphene films released from the catalyst that land on the native substrate (Fig. S6). This is remarkable

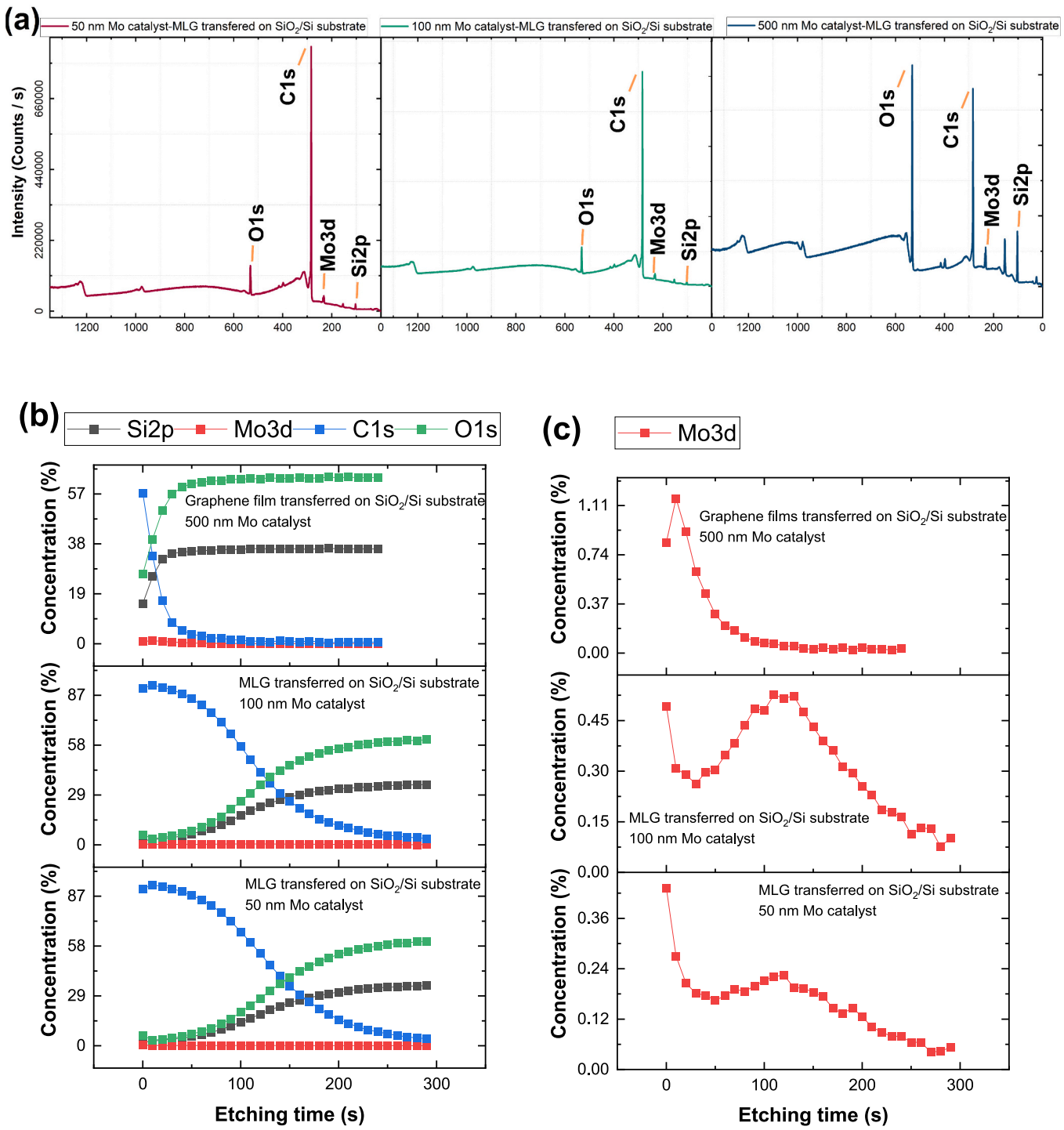

Fig. 9. XPS analysis on transferred graphene films grown on different catalyst thicknesses. a. XPS survey spectra depicting the Si, Mo, C and O peaks. b. XPS depth profiles acquired during a milling process. c. XPS depth profiles of Mo atomic concentration as a function of the etching time.

considering that the graphene layers on the catalyst is faceted and can reconfigure during the catalyst etching and transferring process. The Ra value is even lower for FLG; in this case, no holes contribute to height differences on the surface, and fewer wrinkles are observable.

Regarding the porosity of the transferred MLG (i.e., for the MLG grown on 50 nm and 100 nm Mo catalyst), after the etching process, the MLG suffered an increase in porosity, as indicated in Table 3. The hole density was also calculated before and after the transfer process to estimate the new holes that were created during the transfer step. However, with the high error value on both the porosity and/or the hole density, it is not possible to determine if new holes originate from the transfer process. Then, further studies need to be performed to reduce the uncertainties due to the porosity and hole density and conclude if new pores are created during the transfer step or if these are formed during the catalyst removal. One proposed approach would be to transfer the MLG on a substrate with cavities so the charging effect can be reduced.

Table 2
XPS data analysis on graphene films synthesized on different Mo catalyst thicknesses and subsequently transferred on a SiO_2/Si substrate via a wet method.

Catalyst thickness [nm]	Name	Peak Binding Energy [eV}	FWHM [eV]	Area (P)	Atomic %
50	Si2p	103.32	1.45	6986.7	1.95
	Mo3d	232.37	2.42	18.463.82	0.45
	C1s	283.89	0.77	325.084.95	91.02
	O1s	532.27	2.74	56.682.81	6.57
100	Si2p	102.68	1.51	8628.19	2.38
	Mo3d	231.9	1.52	16.950.66	0.41
	C1s	283.42	0.76	327.227.96	90.53
	O1s	531.78	2.32	58.330.57	6.68
500	Si2p	102.84	1.53	51.110.56	14.78
	Mo3d	232.02	1.3	32.415.58	0.83
	C1s	283.68	0.84	196.571.55	57.01
	O1s	532.09	1.49	228.026.16	27.38

3. Discussion

Graphene formation can be defined as a multifaceted process involving many reactions that can take place simultaneously, and even a competition or balance among these reactions can occur [50]. Thermodynamics and kinetics of the system need to be taken into account to properly describe the graphene growth mechanism via the CVD process

Table 3
Porosity and hole density were calculated from the MLG surface grown using different catalyst thicknesses before and after the transfer process.

	Catalyst thickness [nm]	Catalyst Wet etched	Transferred MLG-wet etched
Porosity [%]	50	0.25 ± 0.19	0.83 ± 0.24
	100	0.22 ± 0.06	1.3 ± 0.6
Hole Density [Number of holes/ μm^2]	50	3.6 ± 1.6	5.6 ± 0.7
	100	5.2 ± 1.7	6.4 ± 5

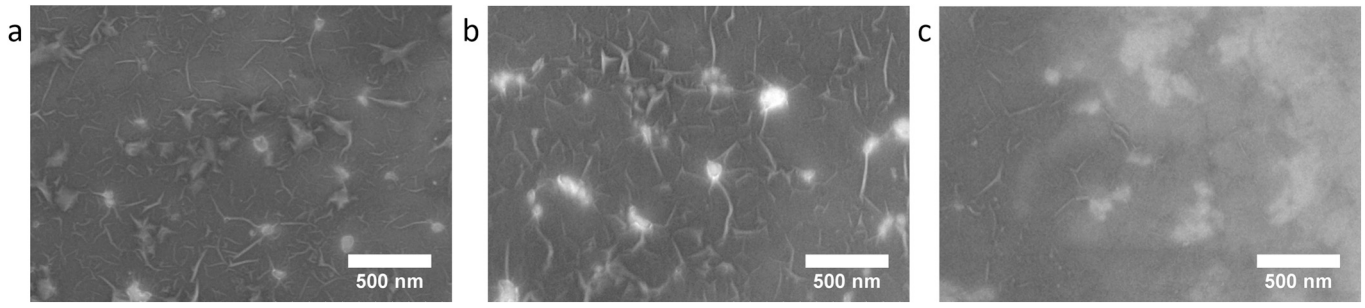

Fig. 10. SEM micrographs of graphene films after a transfer process onto a target substrate. The MLG films were synthesized with different Mo catalyst thicknesses: a 50 nm, b 100 nm, and c 500 nm. Holes appear as bright regions due to the localized electron beam charging of the SiO_2 underneath.

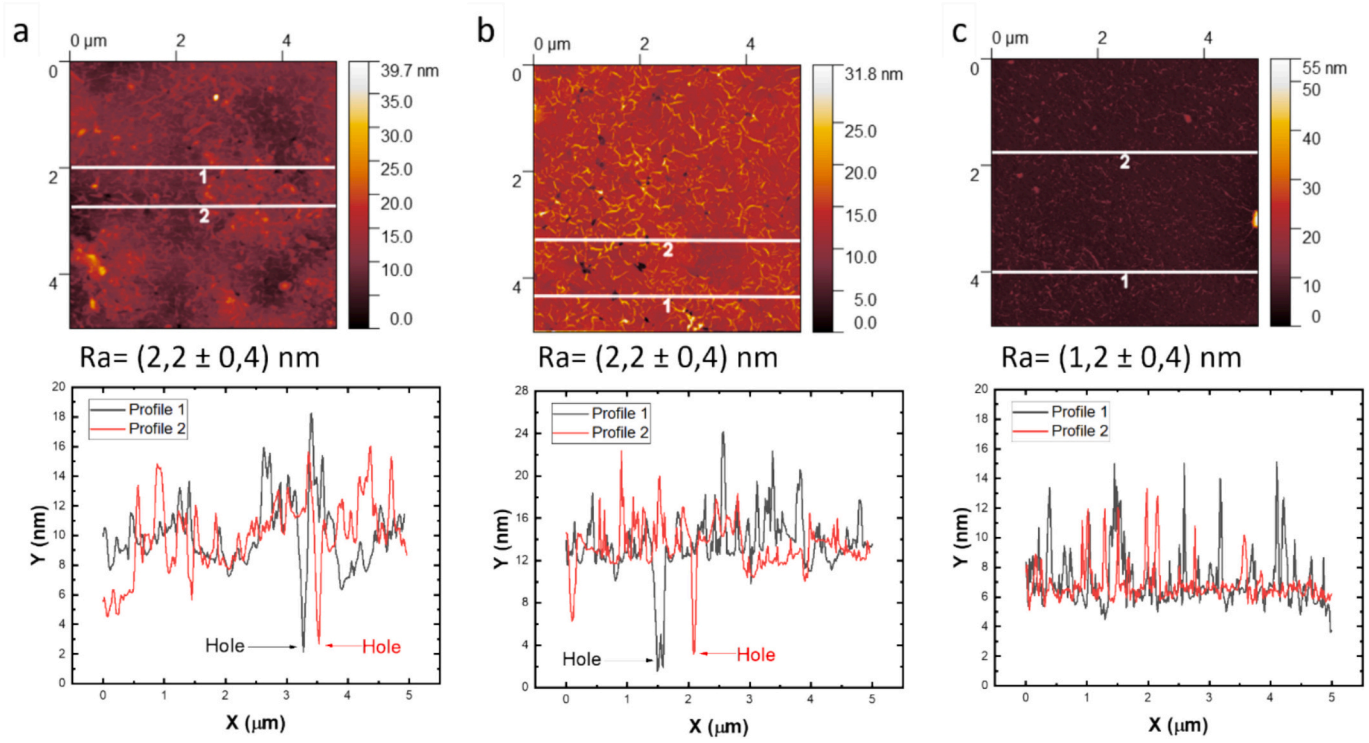

Fig. 11. AFM micrographs of graphene films after a transfer process onto a target substrate. Graphene film have been grown via a CVD process using as Mo catalyst with different thicknesses: a. 50 nm, b. 100 nm, and c. 500 nm. The average Ra value obtained from 3 scans performed at different locations is indicated in each sample.

on metal catalysts [51]. The underlying principle of graphene growth depends on the possibility of the carbon atom reaching a supersaturation state at the metal catalyst surface [52]. Fig. 12.a exemplifies the thermodynamic equilibrium states of the metal catalyst. The supersaturation can be reached by isothermal growth or by precipitation growth. In isothermal growth, the Solvus line is crossed horizontally, implying a constant hydrocarbon feed at a constant temperature. In precipitation growth, the Solvus line is vertically crossed, and then, at a given carbon concentration, once the cooling step begins, a precipitation process occurs. This notion is necessary to describe and understand the graphene formation in this work.

Herein, under the given synthesis conditions, we show that the number of graphene layers can be adjusted by engineering the Mo catalyst sputtered thickness. In particular, we verify that as the catalyst thickness increases, the number of graphene layers synthesized decreases.

This agrees with previous works that reported the synthesis of graphene using Mo as the catalyst. For instance, Wu et al. [21], by optimizing the cooling rate after the feedstock stage, managed to synthesize graphene films ranging from single-layer up to tri-layer, using as a catalyst 100 μm thick Mo foils. Similarly, Zou et al. [27] used foils from groups IVB-VIB metals in graphene growth using the atmospheric pressure CVD process. In this work, it is proven that the best growth results were obtained on group VIB metals, and uniform SL graphene could be grown under the largest synthesis windows, particularly using 25 μm thick Mo foils, even with a large methane concentration (200 sccm) and very slow cooling rate (23 °C/min). If similar growing conditions were applied for Ni or Co foils, MLG or more like-graphitic structures were obtained. This is an interesting property since controlling the kinetics in a wide window of synthesis conditions can allow tuning the desired material properties. Both works stress the fact that the formation of a stable carbide, such as Mo_2C, acts as an interphase layer between the metal and the graphene layer that suppresses carbon segregation or precipitation onto the surface.

In contrast, all the work using as a catalyst Mo thin film (50–90 nm) has reported the synthesis of MLG [7,26,29,53]. The Mo_2C formation might take place at the Mo metal surface as the carbon feedstock is added to the CVD reactor because the formation of this carbide thin layer does not depend on the catalyst thickness. However, the bulk reservoir for the carbon atom diffusion dramatically changes for thin films and thick foils. For instance, Cabrero-Vilatela et al. [54] proposed that the thickness of the catalyst determines the profile length of the potential carbon reservoir, which plays a key role in the kinetic model. The kinetic model can be ascribed by the relation of three different carbon fluxes: J_I defined as the carbon impingement flux, J_G is the graphene growth flux and J_D is the carbon bulk diffusion flux, as illustrated in Fig. 12.b. The thicker the catalyst reservoir, the higher the continued diffusion of carbon atoms that can be absorbed by the metal. Of course, the carbon absorption depends on the permeability of the carbon atom given by the product of solubility, S, and diffusivity, D of the metal catalyst. On the contrary, the thin film catalyst layer will be saturated of carbon faster and the carbon supply will contribute to the graphene formation instead of the diffusion in the metal catalyst.

In the case of Mo thin film catalyst, the cooling rate and Mo_2C layer formation have a very limited impact on the MLG synthesis [55]. If the carbide layer can suppress the precipitation during the cooling state, then it is possible to assume that $J_G \approx J_I$. The number of layers will be dictated by the carbon supply since the catalyst cannot adsorb more carbon atoms. Under this condition, the number of graphene layers may be mainly ruled by the effective synthesis time, as was also verified by Bakhshaee Babaroud et al. [55].

For the graphene grown on Mo foils, the bulk reservoir is a large sink where the carbon atoms can diffuse, and the graphene formation is mediated by the incoming carbon supply and the carbon diffusion into the bulk ($J_G \approx J_I$-J_D). Herein, the precipitation is limited during the cooling stage thanks to the carbide layer between the graphene layer and

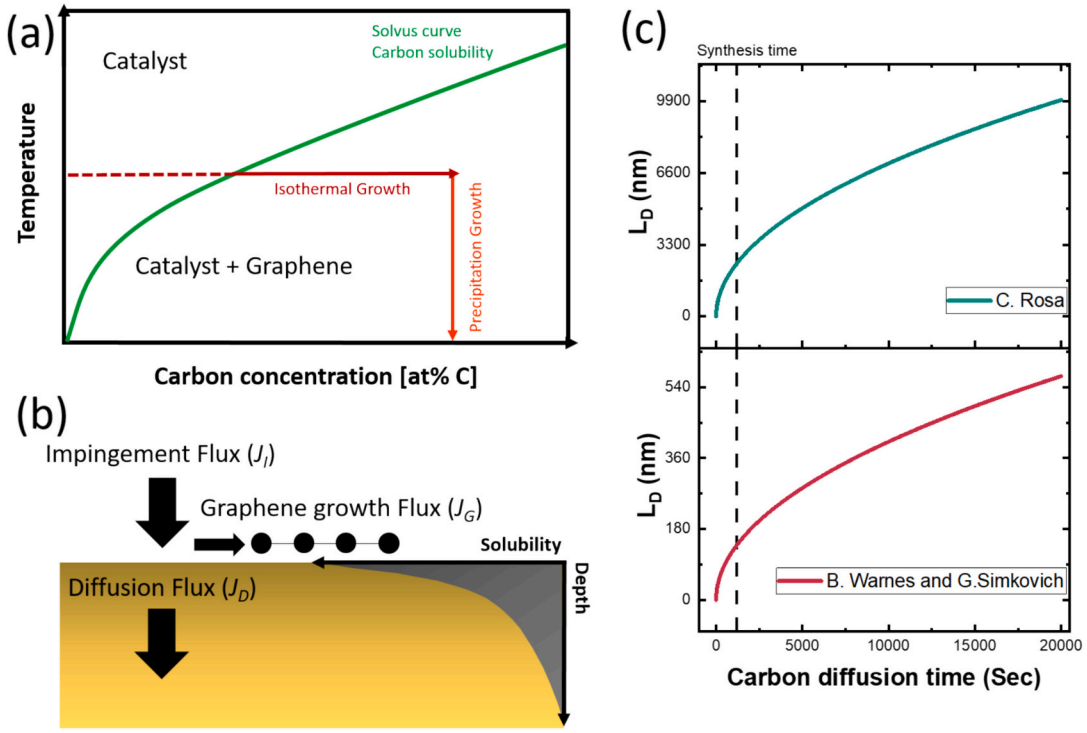

Fig. 12. Summary of the CVD growth process of graphene on catalysts. a Schematic illustration of the metal solid solution phase diagram of the catalyst surface depicting dependence of the carbon solubility with the temperature. The arrows indicate that carbon supersaturation can either be achieved isothermally or by precipitation during the cooling stage. b Carbon fluxes are present during the CVD process, and the resulting carbon diffusion is through the catalyst. c The plot of the characteristic diffusion length of carbon (L_D) as a function of the synthesis time, graph were obtained using the diffusivity values given by B. Warnes and G.Simkovich [58] (red line) and *C. Rosa* [59] (green line).

the catalyst bulk. This was also confirmed by Zou et al. [27] In a control experiment, 300 nm sputtered molybdenum film on SiO2/Si was used for graphene growth, applying the same synthesis conditions as for Mo foils. In this case, MLG were synthesized, attributed to the shortage of molybdenum to trap the excess dissolved carbons.

It is possible to calculate the characteristic diffusion length of carbon (L_D) at a given time. This can give an estimation of the carbon profile length that penetrates through the catalyst, indicating how close the catalyst is to the supersaturation state. Assuming that the carbon diffusion distance increases parabolically with the heating time (t) [56], L_D is given by the Eq. (1):

$$L_D = 2\,(Dt)^{1/2} \quad (1)$$

Of course, the carbon solubility profile in the catalyst might be more complex since defects on the metal catalyst, like grain boundaries, are preferential sites where carbon atoms diffuse. Therefore, for a realistic catalyst, variations of L_D are expected on a given plane. Besides, there is a large distribution in the magnitudes of D reported by different authors of the carbon diffusion on Mo_2C/Mo systems, as it is discussed by Imai et al. [57]. Fig. 12.c shows the plots L_D as time evolves at the heating conditions imposed during the graphene synthesis of the present work, using as a reference the D values calculated by Warnes and G.Simkovich [58] (red line) and *C. Rosa* [59] (green line). Both works were selected to estimate L_D because the diffusion coefficient was extracted at temperatures close to our growth conditions. A huge difference in the carbon concentration values is obtained from these works, but in both cases, the thin catalyst (50 nm and 100 nm) might be completely covered and supersaturated with carbon. This supersaturation state of the Mo catalyst is in harmony with the obtained MLG on these thin film Mo catalysts. Parametric studies are necessary to determine the case of a thick 500 nm Mo catalyst (for instance, if longer growth times can lead to MLG) or the suitable thickness/synthesis conditions to obtain SGL.

In the present work, we also detect the presence of holes in the MLG after the catalyst etching step. It is not possible to attribute the presence of holes to the facetted catalyst structure after the CVD process because, as shown in Fig. 7, the grain size distributions are similar for the three catalyst thicknesses, and the Ra value is also in the same range as shown in Fig. 8. This also could be related to kinetic considerations during the MLG formation. For the growth conditions where $J_D \approx 0$, the incubation time for the nucleation of each new layer might be relatively shorter as there is no mediating diffusion into the catalyst, leading to the formation of a less uniform graphene growth [54]. Then, this inhomogeneous growth can take place because a not appropriate local carbon saturation near the growth surface [60]; in the case of thin films, Mo catalyst (below 100 nm) is very challenging to match with the CVD exposure conditions. This non-uniform growth can lead to an MLG that induces crack propagation or hole formation during the catalyst etching step. However, Raman analysis was not possible to determine that MLG were significantly more defective than the FLG synthesized using a thicker catalyst.

4. Conclusions

The synthesis of MLG films was carried out using the CVD method on Mo-sputtered films with different thicknesses (50 nm, 100 nm and 500 nm). The graphene films grown were characterized at three different configurations: graphene layers with catalyst underneath, catalyst wet etched and graphene films landed on the native substrate, and graphene films transferred to a target substrate. By using three different methods to determine the thickness, this work shows that the number of graphene layers can be adjusted by applying the same synthesis conditions, only varying the Mo catalyst thickness. Increasing the Mo catalyst thickness leads to a reduction in the number of layers. This is attributed to a larger bulk reservoir that can trap carbon atoms. Holes were detected on MLG with a higher number of layers (16 and 25) after the catalyst etching and transfer process but not in the case of the sample with few graphene layers. The transfer-free approach on the thick 500 nm Mo catalyst was not effectively executed within the applied conditions; large amounts of catalyst residues are underneath the FLG and cracks originated on the graphene film structure. The whole generation still needs to be further studied on the MLG. Overall, the present work provides new insights into the synthesis of FLG/MLG using a Mo catalyst. The precise tuning of the FLG/MLG structural properties can be crucial for a large variety of applications based on graphene.

5. Methods

5.1. Graphene film synthesis

Before the catalyst deposition, 600 nm-thick SiO_2 layer was thermally grown on single-crystal silicon wafers (4 in.) with orientation [100] and a resistivity of 5 Ω.cm. A molybdenum (Mo) catalyst was deposited at 50 °C using a SPTS Sigma 204 DC magnetron sputter deposition system. For the catalyst deposition, a Mo target of 332 mm diameter with 99.95 % purity was used, the sputtering power was fixed at 5 kW with a deposition rate of 17.25 nm/s. Three Mo catalyst thickness layers were deposited: 50 nm, 100 nm, and 500 nm. Then, the samples were loaded in an AIXTRON BlackMagic Pro reactor with a cold wall heating system configuration. Before the synthesis step, a pretreatment step was performed using a mixture of Ar and H_2 under a pressure of 25 mbar at 935 °C for 20 min. During the CVD step, 20 sccm of methane (CH_4) as carbon precursor was flown for 20 min. After this time, the CH_4 and H_2 gas flows were stopped and a 1000 sccm Ar flow was set to cool down the sample temperature, with a cooling rate of 3.6 °C/min from 935 °C up to 350 °C, and 0.4 °C/min from 350 °C to room temperature.

5.2. Graphene film transfer

Prior to the graphene film transfer process, the Si wafer holding the stacks of graphene films/Mo/SiO_2 was cut into pieces of approximately 2 cm by 2 cm. The etching agent was a peroxide solution of H_2O_2 concentrated at 31 % (vol.) (D-Basf). The H_2O_2 solution was added until the thickness of the sample was reached leading to Mo etching from the edges to the centre of the sample. The full etching time typically lasts 20 min. Deionized Water (DW) was added to release the graphene layers, which floats on the water. The amount of DW was adjusted to comfortably scoop the graphene film with 3 cm by 3 cm SiO_2 (600 nm)/Si substrate.

5.3. Material characterization

Standard Raman spectroscopy was carried out to access the graphene quality on the graphene films at all different stages (after the CVD synthesis on the native substrate, after the etching process and on the transferred samples onto a target substrate). Raman measurements were performed with a Renishaw inVia Reflex spectrometer coupled with a 532 nm laser source and a 50× objective. In each inspected sample, 5 spectra were obtained to compare the height and centroid position of each peak.

3D Raman surface imaging was made on a similar Renishaw inVia Raman spectroscope with an Andor Newton CCD camera and a 100× objective. For 3D imaging, a map was made of a 20 μm × 20 μm area (indicated by the white dashed line in Fig. 2.a-c) with a resolution of 0.2 μm, resulting in 10,201 measurement points. Each measurement point was taken while maintaining 100 % of the 13.5 mW laser power and two 0.1 s repetitions. Information was collected from areas without graphene, with identical exposure conditions as a reference for the measurement. The reference map was created from 1681 measurement points. For more information on the method leading to 3D imaging, the reader can refer to Dobrowolski et al. [39,40]. Supportive standard

Raman analysis for this stage was carried out on a slightly smaller area inside the 3D imaging field. The measurement was carried out on a 6 μm × 6 μm area (indicated by the red dashed line in Fig. 2.a-c) with a resolution of 0.2 μm, resulting in 961 measurement points. The exposure consisted of two 1 s repetitions at 10 % laser power.

The topography of the MLG was inspected with an NT-MDT NTEGRA AURA atomic force microscope (AFM). The measurements were performed in semi-contact mode at a rate of 0.60 Hz with a scanning area of 5 μm × 5 μm, acquiring 256 lines per map. The AFM images were processed using Gwyddion software where the roughness average (Ra) was calculated [61]. The used tips were PointProbe® Plus (PPP) (purchased at Nanosensors) with a tip radius of curvature <10 nm. For the estimation of the thickness of the transferred layer, a Scanasyst-Air probe (Bruker) was used with a nominal tip radius of 2 nm. The measurements were performed in semi-contact mode at a rate of 0.44 Hz with a scanning area of 10 μm × 10 μm, acquiring 1024 lines per map. The graphene thickness layer was calculated by scanning at the border of the transferred graphene sheets and the target substrate area.

Scanning Electronic Microscope (SEM) Hitachi Regulus 8230 was also used to inspect the MLG surface. The porosity of the MLG was extracted using the open-source "ImageJ" software [62], as similarly detailed in previous reports [63,64]. For the porosity calculation, the image analysis was performed at 5 different spots in each sample using a magnification of 50kX.

High-resolution imaging of the sample's cross-section was performed using a Jeol JEM-2100 Transmission Electron Microscope (TEM) at 200 k*V*. Thin lamellas were obtained by Focused Ion Beam (FIB), using FEI Helios 600 NanoLab Dual Beam Microscope with Omniprobe lift-out system. In the first stage of all lamellas preparation, the selected surfaces of each sample were protected by two-step deposition process using dual beam SEM/FIB system. The first protective strip was deposited with electrons, but the top one (thicker than the first one) with gallium ions. The sizes of deposited strips were about 20 μm (length) and 3 μm (wide), with summarized thickness of 2.5 μm. The beam parameters during protective strips deposition were 3 kV (beam energy) and 2.7 nA (beam current) for the electron-beam. However, for ion-beam deposition the beam parameters were 30 kV and 0.9 nA. Other FIB processes leading to TEM lamellas thinning were performed using ion-beam energy of 30 kV and an ion-beam current ranging from nano-amperes to picoamperes.

X-ray Photoelectron Spectroscopy (XPS) was used to analyse the presence of residues underneath the MLG film after the catalyst etching steps. The XPS measurements were executed in a K-Alpha system manufactured by ThermoFisher. The spot size was 400 μm. XPS depth profiles were acquired using the K-Alpha source with a power of 20 W. The samples were ion-milled over an area of 2 mm × 3 mm with Ar + ions at an energy of 2000 V at 10 μA.

CRediT authorship contribution statement

Leandro Nicolas Sacco: Writing – review & editing, Writing – original draft, Visualization, Validation, Supervision, Project administration, Methodology, Investigation, Funding acquisition, Formal analysis, Data curation, Conceptualization. **Artur Dobrowolski:** Writing – review & editing, Investigation, Funding acquisition, Formal analysis, Data curation. **Bart Boshuizen:** Methodology, Data curation. **Jakub Jagiełło:** Methodology, Data curation. **Beata Pyrzanowska:** Methodology, Investigation. **Adam Łaszcz:** Methodology, Data curation. **Tymoteusz Ciuk:** Investigation, Data curation. **Sten Vollebregt:** Writing – review & editing, Validation, Project administration, Funding acquisition, Formal analysis, Data curation, Conceptualization.

Declaration of competing interest

The authors declare no competing financial or non-financial interests.

Acknowledgements

L. Sacco and S. Vollebregt would like to thank Else Kooi Lab staff (Delft University of Technology) for the processing support.

The research leading to these results has received funding from the National Centre for Research and Development, Poland, under Grant Agreement No. M-ERA.NET3/2021/83/I4BAGS/2022 for project "Ion Implantation for Innovative Interface modifications in BAttery and Graphene-enabled Systems". The M-ERA.NET3 has received funding from the European Union's Horizon 2020 Research and Innovation Programme under Grant Agreement No. 958174.

3D Raman surface imaging method has received funding from the National Science Centre, Poland, under Grant Agreement No. OPUS 2019/33/B/ST3/02677 for project "Influence of the silicon carbide and the dielectric passivation defect structure on high-temperature electrical properties of epitaxial graphene".

Appendix A. Supplementary data

Supplementary data to this article can be found online at https://doi.org/10.1016/j.diamond.2025.112195.

Data availability

The data that support the findings of this work are available from the corresponding author upon reasonable request.

References

[1] B. Deng, Z. Liu, H. Peng, Toward mass production of CVD graphene films, Adv. Mater. 31 (2019) 1800996, https://doi.org/10.1002/adma.201800996.
[2] Y. Song, W. Zou, Q. Lu, L. Lin, Z. Liu, Graphene transfer: paving the road for applications of chemical vapor deposition graphene, Small n/a (2021) 2007600, https://doi.org/10.1002/smll.202007600.
[3] L.-P. Ma, W. Ren, H.-M. Cheng, Transfer methods of graphene from metal substrates: a review, Small Methods 3 (2019) 1900049, https://doi.org/10.1002/smtd.201900049.
[4] J. Ning, D. Wang, Y. Chai, X. Feng, M. Mu, L. Guo, J. Zhang, Y. Hao, Review on mechanism of directly fabricating wafer-scale graphene on dielectric substrates by chemical vapor deposition, Nanotechnology 28 (2017) 284001, https://doi.org/10.1088/1361-6528/aa6c08.
[5] H. Wang, G. Yu, Direct CVD graphene growth on semiconductors and dielectrics for transfer-free device fabrication, Adv. Mater. 28 (2016) 4956–4975, https://doi.org/10.1002/adma.201505123.
[6] C.-Y. Su, A.-Y. Lu, C.-Y. Wu, Y.-T. Li, K.-K. Liu, W. Zhang, S.-Y. Lin, Z.-Y. Juang, Y.-L. Zhong, F.-R. Chen, et al., Direct formation of wafer scale graphene thin layers on insulating substrates by chemical vapor deposition, Nano Lett. 11 (2011) 3612–3616, https://doi.org/10.1021/nl201362n.
[7] S. Vollebregt, B. Alfano, F. Ricciardella, A.J.M. Giesbers, Y. Grachova, H.W.V. Zeijl, T. Polichetti, P.M. Sarro, A transfer-free wafer-scale CVD graphene fabrication process for MEMS/NEMS sensors, in: Proceedings of the 2016 IEEE 29th International Conference on Micro Electro Mechanical Systems (MEMS), 2016, pp. 17–20.
[8] H. Choi, Y. Lim, M. Park, S. Lee, Y. Kang, M.S. Kim, J. Kim, M. Jeon, Precise control of chemical vapor deposition graphene layer thickness using NixCu1−x alloys, J. Mater. Chem. C 3 (2015) 1463–1467, https://doi.org/10.1039/C4TC01979B.
[9] B. Huet, J.-P. Raskin, D.W. Snyder, J.M. Redwing, Fundamental limitations in transferred CVD graphene caused by cu catalyst surface morphology, Carbon 163 (2020) 95–104, https://doi.org/10.1016/j.carbon.2020.02.074.
[10] Q. Yu, L.A. Jauregui, W. Wu, R. Colby, J. Tian, Z. Su, H. Cao, Z. Liu, D. Pandey, D. Wei, et al., Control and characterization of individual grains and grain boundaries in graphene grown by chemical vapour deposition, Nat. Mater. 10 (2011) 443–449, https://doi.org/10.1038/nmat3010.
[11] P.L. L., B. Federico, A. Cristina, D. Carlo, S. German, M.M. M., P. Maria, C. Giovanni, Real-time imaging of adatom-promoted graphene growth on nickel, Science 359 (2018) 1243–1246, https://doi.org/10.1126/science.aan8782.
[12] M.R. Habib, T. Liang, X. Yu, X. Pi, Y. Liu, M. Xu, A review of theoretical study of graphene chemical vapor deposition synthesis on metals: nucleation, growth, and the role of hydrogen and oxygen, Rep. Prog. Phys. 81 (2018) 36501, https://doi.org/10.1088/1361-6633/aa9bbf.
[13] X. Li, W. Cai, L. Colombo, R.S. Ruoff, Evolution of graphene growth on Ni and cu by carbon isotope labeling, Nano Lett. 9 (2009) 4268–4272, https://doi.org/10.1021/nl902515k.
[14] W.E. Few, G.K. Manning, Solubility of carbon and oxygen in molybdenum, JOM 4 (1952) 271–274.

[15] A.A. Pakhnevich, S.V. Golod, V.Y. Prinz, Surface melting of copper during graphene growth by chemical vapour deposition, J. Phys. D Appl. Phys. 48 (2015) 435303, https://doi.org/10.1088/0022-3727/48/43/435303.
[16] H. Hu, K. Xia, S. Zhao, M. Ma, Q. Zheng, Eliminating graphene wrinkles by strain engineering, Extreme Mech. Lett. 42 (2021) 101104, https://doi.org/10.1016/j.eml.2020.101104.
[17] J.J. Lander, H.E. Kern, A.L. Beach, Solubility and diffusion coefficient of carbon in nickel: reaction rates of nickel-carbon alloys with barium oxide, J. Appl. Phys. 23 (1952) 1305–1309, https://doi.org/10.1063/1.1702064.
[18] J.C. Shelton, H.R. Patil, J.M. Blakely, Equilibrium segregation of carbon to a nickel (111) surface: a surface phase transition, Surf. Sci. 43 (1974) 493–520, https://doi.org/10.1016/0039-6028(74)90272-6.
[19] F. Ricciardella, S. Vollebregt, E. Kurganova, A.J.M. Giesbers, M. Ahmadi, P. M. Sarro, Growth of multi-layered graphene on molybdenum catalyst by solid phase reaction with amorphous carbon, 2D Materials 6 (2019) 35012, https://doi.org/10.1088/2053-1583/ab1518.
[20] Y. Grachova, S. Vollebregt, A.L. Lacaita, P.M. Sarro, High quality wafer-scale CVD graphene on molybdenum thin film for sensing application, Procedia Engineering 87 (2014) 1501–1504, https://doi.org/10.1016/j.proeng.2014.11.583.
[21] Y. Wu, G. Yu, H. Wang, B. Wang, Z. Chen, Y. Zhang, B. Wang, X. Shi, X. Xie, Z. Jin, et al., Synthesis of large-area graphene on molybdenum foils by chemical vapor deposition, Carbon 50 (2012) 5226–5231, https://doi.org/10.1016/j.carbon.2012.07.007.
[22] P. Wang, D. Wang, S. Mondal, M. Hu, Y. Wu, T. Ma, Z. Mi, Ferroelectric nitride Heterostructures on CMOS compatible molybdenum for synaptic Memristors, ACS Appl. Mater. Interfaces 15 (2023) 18022–18031, https://doi.org/10.1021/acsami.2c22798.
[23] L.N. Sacco, H. Meng, S. Vollebregt, Humidity sensor based on multi-layer graphene (MLG) integrated onto a micro-hotplate (MHP), in: Proceedings of the 2022 IEEE Sensors, 2022, pp. 1–4.
[24] J. Romijn, S. Vollebregt, H.W.V. Zeijl, P.M. Sarro, A wafer-scale process for the monolithic integration of CVD graphene and CMOS logic for smart MEMS/NEMS sensors, in: Proceedings of the 2019 IEEE 32nd International Conference on Micro Electro Mechanical Systems (MEMS), 2019, pp. 260–263.
[25] J. Romijn, R.J. Dolleman, M. Singh, H.S.J. van der Zant, P.G. Steeneken, P. M. Sarro, S. Vollebregt, Multi-layer graphene pirani pressure sensors, Nanotechnology 32 (2021) 335501, https://doi.org/10.1088/1361-6528/abff8e.
[26] F. Ricciardella, S. Vollebregt, B. Boshuizen, F.J.K. Danzl, I. Cesar, P. Spinelli, P. M. Sarro, Wafer-scale transfer-free process of multi-layered graphene grown by chemical vapor deposition, Materials Research Express 7 (2020) 35001, https://doi.org/10.1088/2053-1591/ab771e.
[27] Z. Zou, L. Fu, X. Song, Y. Zhang, Z. Liu, Carbide-forming groups IVB-VIB metals: a new territory in the periodic table for CVD growth of graphene, Nano Lett. 14 (2014) 3832–3839, https://doi.org/10.1021/nl500994m.
[28] C.-M. Seah, S.-P. Chai, A.R. Mohamed, Mechanisms of graphene growth by chemical vapour deposition on transition metals, Carbon 70 (2014) 1–21, https://doi.org/10.1016/j.carbon.2013.12.073.
[29] S.K. Bijkerk, B. Wesley van den, S. Bart, K. Robbert van de, B. Jos, Fred., The role of pinhole structures in Mo thin films on multi-layer graphene synthesis, J. Phys.: Materials 3 (2020) 025004.
[30] A.C. Ferrari, J.C. Meyer, V. Scardaci, C. Casiraghi, M. Lazzeri, F. Mauri, S. Piscanec, D. Jiang, K.S. Novoselov, S. Roth, et al., Raman Spectrum of graphene and graphene layers, Phys. Rev. Lett. 97 (2006) 187401, https://doi.org/10.1103/PhysRevLett.97.187401.
[31] Y. Hwangbo, C.-K. Lee, A.E. Mag-Isa, J.-W. Jang, H.-J. Lee, S.-B. Lee, S.-S. Kim, J.-H. Kim, Interlayer non-coupled optical properties for determining the number of layers in arbitrarily stacked multilayer graphenes, Carbon 77 (2014) 454–461, https://doi.org/10.1016/j.carbon.2014.05.050.
[32] V. Kumar, A. Kumar, D.-J. Lee, S.-S. Park, Estimation of number of graphene layers using different methods: a focused review, Materials 14 (2021) 4590.
[33] A.C. Ferrari, D.M. Basko, Raman spectroscopy as a versatile tool for studying the properties of graphene, Nat. Nanotechnol. 8 (2013) 235–246, https://doi.org/10.1038/nnano.2013.46.
[34] Y. Hao, Y. Wang, L. Wang, Z. Ni, Z. Wang, R. Wang, C.K. Koo, Z. Shen, J.T. L. Thong, Probing layer number and stacking order of Few-layer graphene by Raman spectroscopy, Small 6 (2010) 195–200, https://doi.org/10.1002/smll.200901173.
[35] L.M. Malard, M.A. Pimenta, G. Dresselhaus, M.S. Dresselhaus, Raman spectroscopy in graphene, Phys. Rep. 473 (2009) 51–87, https://doi.org/10.1016/j.physrep.2009.02.003.
[36] R.P. Vidano, D.B. Fischbach, L.J. Willis, T.M. Loehr, Observation of Raman band shifting with excitation wavelength for carbons and graphites, Solid State Commun. 39 (1981) 341–344.
[37] C.J. Shearer, A.D. Slattery, A.J. Stapleton, J.G. Shapter, C.T. Gibson, Accurate thickness measurement of graphene, Nanotechnology 27 (2016) 125704, https://doi.org/10.1088/0957-4484/27/12/125704.
[38] Z.H. Ni, H.M. Wang, J. Kasim, H.M. Fan, T. Yu, Y.H. Wu, Y.P. Feng, Z.X. Shen, Graphene thickness determination using reflection and contrast spectroscopy, Nano Lett. 7 (2007) 2758–2763, https://doi.org/10.1021/nl071254m.
[39] A. Dobrowolski, J. Jagiełło, D. Czołak, T. Ciuk, Determining the number of graphene layers based on Raman response of the SiC substrate, Physica E 134 (2021) 114853, https://doi.org/10.1016/j.physe.2021.114853.
[40] A. Dobrowolski, J. Jagiełło, T. Ciuk, K. Piętak, E.B. Możdżyńska, Layer-resolved Raman imaging and analysis of parasitic ad-layers in transferred graphene, Appl. Surf. Sci. 608 (2023) 155054, https://doi.org/10.1016/j.apsusc.2022.155054.
[41] D. Pandey, S. Xiao, M. Wubs, Graphene multilayers for coherent perfect absorption: effects of interlayer separation, Opt. Express 30 (2022) 44504–44517, https://doi.org/10.1364/OE.475046.
[42] M.S. Alam, J. Lin, M. Saito, First-principles calculation of the interlayer distance of the two-layer graphene, Jpn. J. Appl. Phys. 50 (2011) 080213, https://doi.org/10.1143/JJAP.50.080213.
[43] Á. Peña, J. López-Sánchez, L. Sacco, S. Vollebregt, J. Marqués-Marchán, M. C. Horrillo, P. Marín, D. Matatagui, Beyond conventional characterization: defect engineering role for sensitivity and selectivity of room-temperature UV-assisted graphene-based NO_2 sensors, Talanta 286 (2025) 127507, https://doi.org/10.1016/j.talanta.2024.127507.
[44] C.-C. Chan, W.-L. Chung, W.-Y. Woon, Nucleation and growth kinetics of multi-layered graphene on copper substrate, Carbon 135 (2018) 118–124, https://doi.org/10.1016/j.carbon.2018.04.044.
[45] D. Chen, M. Liu, L. Yin, T. Li, Z. Yang, X. Li, B. Fan, H. Wang, R. Zhang, Z. Li, et al., Single-crystalline MoO3 nanoplates: topochemical synthesis and enhanced ethanol-sensing performance, J. Mater. Chem. 21 (2011) 9332–9342, https://doi.org/10.1039/C1JM11447F.
[46] M. Dieterle, G. Weinberg, G. Mestl, Raman spectroscopy of molybdenum oxides part I. Structural characterization of oxygen defects in MoO3−x by DR UV/VIS, Raman spectroscopy and X-ray diffraction, Phys. Chem. Chem. Phys. 4 (2002) 812–821, https://doi.org/10.1039/B107012F.
[47] J.-L. Wree, D. Rogalla, A. Ostendorf, K.D. Schierbaum, A. Devi, Plasma-enhanced atomic layer deposition of molybdenum oxide thin films at low temperatures for hydrogen gas sensing, ACS Appl. Mater. Interfaces (2023), https://doi.org/10.1021/acsami.2c19827.
[48] D. Geng, X. Zhao, Z. Chen, W. Sun, W. Fu, J. Chen, W. Liu, W. Zhou, K.P. Loh, Direct synthesis of large-area 2D Mo2C on in situ grown graphene, Adv. Mater. 29 (2017) 1700072, https://doi.org/10.1002/adma.201700072.
[49] F. Ricciardella, S. Vollebregt, R. Tilmann, O. Hartwig, C. Bartlam, P.M. Sarro, H. Sachdev, G.S. Duesberg, Influence of defect density on the gas sensing properties of multi-layered graphene grown by chemical vapor deposition, Carbon Trends 3 (2021) 100024, https://doi.org/10.1016/j.cartre.2021.100024.
[50] F. Bonaccorso, A. Lombardo, T. Hasan, Z. Sun, L. Colombo, A.C. Ferrari, Production and processing of graphene and 2d crystals, Mater. Today 15 (2012) 564–589, https://doi.org/10.1016/S1369-7021(13)70014-2.
[51] J. Zhang, F. Wang, V.B. Shenoy, M. Tang, J. Lou, Towards controlled synthesis of 2D crystals by chemical vapor deposition (CVD), Mater. Today 40 (2020) 132–139, https://doi.org/10.1016/j.mattod.2020.06.012.
[52] M.H. Ani, M.A. Kamarudin, A.H. Ramlan, E. Ismail, M.S. Sirat, M.A. Mohamed, M. A. Azam, A critical review on the contributions of chemical and physical factors toward the nucleation and growth of large-area graphene, J. Mater. Sci. 53 (2018) 7095–7111, https://doi.org/10.1007/s10853-018-1994-0.
[53] S. Kizir, W.T.E. van den Beld, B. Schurink, R.W.E. van de Kruijs, J.P.H. Benschop, F. Bijkerk, Bifunctional catalytic effect of Mo2C/oxide interface on multi-layer graphene growth, Sci. Rep. 11 (2021) 15377, https://doi.org/10.1038/s41598-021-94694-4.
[54] A. Cabrero-Vilatela, R.S. Weatherup, P. Braeuninger-Weimer, S. Caneva, S. Hofmann, Towards a general growth model for graphene CVD on transition metal catalysts, Nanoscale 8 (2016) 2149–2158, https://doi.org/10.1039/C5NR06873H.
[55] N. Bakhshaee Babaroud, M. Palmar, A.I. Velea, C. Coletti, S. Weingärtner, F. Vos, W.A. Serdijn, S. Vollebregt, V. Giagka, Multilayer CVD graphene electrodes using a transfer-free process for the next generation of optically transparent and MRI-compatible neural interfaces, Microsyst. Nanoeng. 8 (2022) 107, https://doi.org/10.1038/s41378-022-00430-x.
[56] Y. Hiraoka, H. Iwasawa, T. Inoue, M. Nagae, J. Takada, Application of fractography to the study of carbon diffusion in molybdenum, J. Alloys Compd. 377 (2004) 127–132, https://doi.org/10.1016/j.jallcom.2004.01.042.
[57] J.-I. Imai, O. Taguchi, G.P. Tiwari, Y. Iijima, Diffusion of carbon in niobium and molybdenum, Mater. Trans. 55 (2014) 1786–1791.
[58] B.M. Warnes, G. Simkovich, Carbon diffusivity in Mo2C from 800 to 1000 °C, Journal of the Less Common Metals 106 (1985) 241–249, https://doi.org/10.1016/0022-5088(85)90259-0.
[59] C.J. Rosa, Carbon diffusion in Mo2C as determined from carburization of Mo, Metall. Trans. A. 14 (1983) 199–202, https://doi.org/10.1007/BF02651616.
[60] R.S. Weatherup, B. Dlubak, S. Hofmann, Kinetic control of catalytic CVD for high-quality graphene at low temperatures, ACS Nano 6 (2012) 9996–10003, https://doi.org/10.1021/nn303674g.
[61] D. Nečas, P. Klapetek, Gwyddion: an open-source software for SPM data analysis, Open Physics 10 (2012) 181–188.
[62] C.A. Schneider, W.S. Rasband, K.W. Eliceiri, NIH image to ImageJ: 25 years of image analysis, Nat. Methods 9 (2012) 671–675, https://doi.org/10.1038/nmeth.2089.
[63] L. Sacco, I. Florea, C.-S. Cojocaru, Fabrication of porous anodic alumina (PAA) templates with straight pores and with hierarchical structures through exponential voltage decrease technique, Surf. Coat. Technol. 364 (2019) 248–255, https://doi.org/10.1016/j.surfcoat.2019.02.086.
[64] L. Sacco, I. Florea, M. Châtelet, C.-S. Cojocaru, Investigation of porous anodic alumina templates formed by anodization of single-crystal aluminum substrates, Thin Solid Films 660 (2018) 213–220, https://doi.org/10.1016/j.tsf.2018.06.015.